


Birefringence of Single Polarization for Flexural-Wave Metamaterials

Yan Meng¹,† Yiran Hao¹,† Liyou Luo, and Jensen Li¹*

Department of Physics, The Hong Kong University of Science and Technology, Clear Water Bay, Hong Kong, China

 (Received 27 August 2022; revised 7 November 2022; accepted 22 November 2022; published 23 December 2022)

The concept of birefringence, commonly treated as a property resulting from more than one polarization, is associated with different refractive indices, depending on polarization. Here, we propose a two-dimensional elastic metamaterial engineered to demonstrate birefringence of single polarization for flexural waves. By adopting a network of beams with “overpass” structures to upset the topology of unit cells from a conventional elastic plate, birefringence of single polarization at low frequencies can be realized and confirmed through measured band structures and double refraction of the flexural waves; this is further supported by full-wave simulations and models. Our approach can engineer birefringence at low frequencies in which the wavelength is at least a few times larger than the lattice constant, further allowing efficient control of beam splitting, filtering, and multiplexing with applications for elastic wave devices.

DOI: [10.1103/PhysRevApplied.18.064073](https://doi.org/10.1103/PhysRevApplied.18.064073)

I. INTRODUCTION

Metamaterials, which are constructed from artificially designed microstructures, often possess counterintuitive wave properties beyond those of conventional composite materials. The concept of a metamaterial is useful in various regimes of classical waves. In electromagnetics, many intriguing phenomena, such as negative refractive indices [1,2], zero refractive indices [3], cloaking [4,5], and analog black holes [6], can be investigated with metamaterials. In acoustics, there have been huge efforts to extend these concepts [7–9] and use drastically different design strategies due to the different natures of waves that are needed [10–15]. While many demonstrations in acoustic metamaterials are for airborne sound with scalar-wave propagation, the concept of a metamaterial has been gradually extended to elastic waves in solids, where three polarizations (one longitudinal and two transverse polarizations) need to be considered. In this case, the constitutive relationship and wave phenomena unavoidably become more complicated, such as Willis coupling and mode conversion, while the physics involved can become richer due to the interplay of different polarizations [16–25]. Recently, geometric nonlocalities, containing intentional connections for long-range interactions, have been shown to be an effective way to engineer dispersion at low frequencies, e.g., to obtain rotonlike dispersion or angular functionality for elastic metamaterials [26–28]. Different approaches for constructing resonances, counterintuitive constitutive parameters, and achieving tunability

for elastic-wave metamaterials are in rapid development [29–31], and thus, may find useful applications in nondestructive testing and surface-acoustic-wave devices.

Birefringence in electromagnetism describes an incident light being split by a material into two refractive beams with different propagation directions [32,33]. A birefringent metamaterial thus provides a straightforward way to control the amplitude, phase, and polarization of the incident beam [34–39], which can be immediately useful for the construction of various optical devices, e.g., filters [40], modulators [41], and sensors [42]. Birefringence comes from the fact that the refractive index of the material depends on polarization, e.g., between two orthogonal linear polarizations for an anisotropic material or between two opposite circular polarizations for a chiral material in optics. The concept can be extended to the case of elastic waves in a solid, e.g., between the S_0 and A_0 lamb modes on an elastic plate [21]. Birefringence is, therefore, usually a concept for when we have more than one polarization. On the other hand, if we can work at higher frequencies, birefringence for scalar acoustic waves can be obtained through band folding in the diffraction regime at higher-frequency bands [43]. To work at low frequencies, at which the wavelength is much longer than the lattice constant, a recent theoretical proposal is that birefringence at low frequencies can be achieved with two parallel layers of pipe networks with acoustic waves propagating in either layer, although how the structures can be used and integrated with a background acoustic medium has to be further explored [44]. This will allow us to engineer dispersion relationships at low frequencies and promote their usage to design further devices. It is also worth mentioning that another concept originating from

*jensenli@ust.hk

†Y. Meng and Y. Hao contributed equally to this work.

more than one polarization, spin-orbit coupling, can now be implemented in scalar acoustic waves through the special topological arrangement of air channels [45], leading to the question of whether some of the other concepts conventionally originating from more than one polarizations can be achieved for scalar waves as well.

Here, we experimentally realize the concept of birefringence of single polarization at low frequencies in terms of flexural waves on a metamaterial plate. We adopt an “overpass” approach using bridges in intentionally connecting waves at different locations of each unit cell [46]. This results in a flexural-wave metamaterial that can be mechanically well supported and the metamaterial is able to be integrated naturally in a background medium of a homogeneous plate. As we show in Sec. II, such a mechanism in generating birefringence of single polarization relies on upsetting the topology of each unit cell. As a result, the birefringence of single polarization can be engineered at an arbitrary low frequency if needed, in which the wavelength in the background medium is at least a few times larger than the lattice constant. As the birefringence of single polarization occurs within the flexural mode instead of two polarizations of very different spatial symmetries, it will be easier to control the power efficiency; this is potentially useful for applications in designing elastic wave components with filtering, beam splitting, or multiplexing capabilities.

II. DESIGN AND MODELING OF BIREFRINGENT METAMATERIALS

The top view of the proposed flexural-wave metamaterial is shown in Fig. 1(a). The black dashed box indicates a square unit cell, which contains two orthogonal arched beams (yellow) connected to a supporting frame (orange). The intersections between the arched beams and the supporting frames are denoted as “B,” “C,” and “D,” respectively. In addition, there is an overpass between the two arched beams at position “A,” where the two beams are not connected but with a gap of 1 mm. Another choice in defining a unit cell is denoted by the red dashed square, with its perspective view and top view, respectively, shown in the upper and lower panels in Fig. 1(b). Its geometry parameters are correspondingly labeled. The unit cell has a lattice constant a . The arched beams have thicknesses of h_0 at the boundaries and t_0 (less than h_0) at the center and have a width of l . Each thin beam in the supporting frames (orange) has a width of b and a thickness of g . The dimensions are chosen to be $a = 14$ mm, $l = 3$ mm, $h_0 = 3$ mm, and $t_0 = 1$ mm. The metamaterial is made of cured photosensitive resin [using three-dimensional (3D) printing] with the following properties: density $\rho_0 = 1190$ kg m $^{-3}$, Young’s modulus $E_0 = 3.4$ GPa, and Poisson ratio $\nu = 0.35$, which are extracted by measuring the propagation

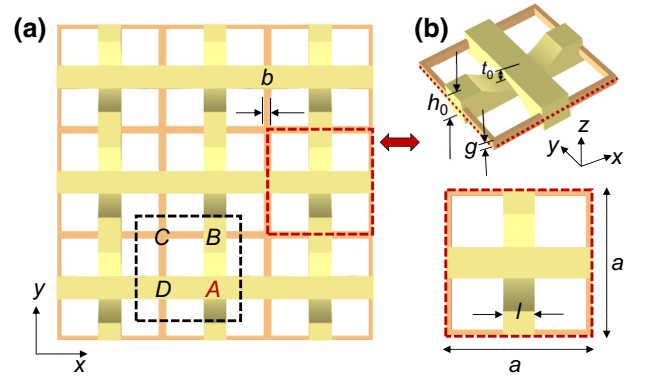


FIG. 1. (a) Top view of the flexural-wave metamaterial. Choice of unit cell is denoted by the black dashed square with three intersections marked by B, C, and D; an overpass is denoted by position A, where the two arched beams (yellow) are not connected. Another choice of unit cell is denoted by the red dashed square; its perspective and top views are shown in the upper and lower panels in (b). Unit cell of the metamaterial is composed of two arched beams and a supporting frame (orange), and its lattice constant is $a = 14$ mm. Each thin beam in the supporting frame has a thickness of g and a width of b . Each arched beam has a width of $l = 3$ mm, and a thickness of $t_0 = 1$ mm in the middle and $h_0 = 3$ mm at both ends. At the center of a unit cell, the gap between two arched beams is 1 mm.

constants of flexural modes of a homogeneous beam made of the same material [47].

Our metamaterial is effectively constructed from a network of beams lying on the x - y plane. The flexural waves propagating along a beam section of thickness h in direction $\alpha = x$ or y can be described by Euler-Bernoulli beam theory (with harmonic $e^{-i\omega t}$ dependence with angular frequency ω) as

$$-i\Pi\partial_\alpha \begin{pmatrix} u_z \\ \partial_z u_\alpha \\ M_{\alpha\alpha} \\ Q_\alpha \end{pmatrix} = H \begin{pmatrix} u_z \\ \partial_z u_\alpha \\ M_{\alpha\alpha} \\ Q_\alpha \end{pmatrix}, \quad (1)$$

where

$$\Pi = \begin{pmatrix} 0 & 0 & 0 & -i \\ 0 & 0 & -i & 0 \\ 0 & i & 0 & 0 \\ i & 0 & 0 & 0 \end{pmatrix},$$

$$H = \begin{pmatrix} \omega^2 \rho_0 b_\alpha h & 0 & 0 & 0 \\ 0 & 0 & 0 & -1 \\ 0 & 0 & \frac{1}{E_0 l_\alpha} & 0 \\ 0 & -1 & 0 & 0 \end{pmatrix},$$

and i is the imaginary unit. u_α is the displacement along the α direction. $M_{\alpha\alpha} = b_\alpha \int z \sigma_{\alpha\alpha} dz$ is the bending moment, $\sigma_{\alpha\alpha}$ is the $\alpha\alpha$ component of the stress tensor. $Q_\alpha = b_\alpha \int \sigma_{\alpha z} dz$ is the shear force. $b_\alpha = l$ for the arched

beams; $b_\alpha = b$ for the beams of the supporting frame. $I_\alpha = b_\alpha h^3/12$ is the geometric moment of inertia. For a beam of length L , we can integrate Eq. (1) to obtain the transfer matrix as

$$T = e^{iL\Pi H}, \quad (2)$$

which transfers the fields u_z , $\partial_z u_\alpha$, $M_{\alpha\alpha}$, and Q_α across the beam length. We note that, for an arched beam with varying thickness, Eq. (2) is cascaded from different sections of constant thicknesses in transferring the fields as approximation. At a particular junction at B , C , or D , if we use superscripts “(L),” “(R),” “(T),” and “(B)” to indicate the fields located at the left, right, top, and bottom of the junction, respectively, the continuity equation at the junction can be expressed as

$$\begin{aligned} u_z^{(L)} &= u_z^{(R)} = u_z^{(T)} = u_z^{(B)}, \\ \partial_z u_x^{(L)} &= \partial_z u_x^{(R)}, \quad \partial_z u_y^{(T)} = \partial_z u_y^{(B)}, \\ M_{xx}^{(L)} &= M_{xx}^{(R)}, \quad M_{yy}^{(T)} = M_{yy}^{(B)}, \\ Q_x^{(L)} + Q_y^{(B)} &= Q_x^{(R)} + Q_y^{(T)}. \end{aligned} \quad (3)$$

The first two formulas in Eq. (3) indicate the continuity of the displacement fields, while the other two formulas express the balance of forces at the junction. Finally, to obtain the model band structure of the metamaterial, Eqs. (2) and (3) are combined to propagate the fields to the boundary of the unit cell (black dashed square in Fig. 1) at which the Bloch boundary condition is further applied with wave vector $\mathbf{k} = k_x \hat{x} + k_y \hat{y}$.

The band structures for flexural waves of our proposed metamaterial can be extracted from the analytical model. The results of the first two bands for $g = b = 0.5$, 0.75 , and 1 mm are plotted in Figs. 2(d)–2(f), respectively; the first band is indicated by the green curve and the second

band is indicated by the blue curve. We pick the modes dominated by vertical displacements in model and simulations. As can be seen, there are two birefringent flexural modes below 4.5 kHz, with the bottom of the second band approaching a lower frequency as the width of the beams of the supporting frame decreases. For comparison, we also plot the band structures obtained from full-wave simulations (COMSOL Multiphysics), as indicated by the star symbols, showing an accurate representation of the model band structure. We note that the higher bands (not plotted in Fig. 2) are beyond the capability of the model. These results confirm the birefringence of the flexural mode in the long-wavelength regime. In practice, we need a frame with finite g and b to support the whole metamaterial. The supporting frame, unlike the scalar acoustic design [44], enforces a background “matrix” to connect the arched beams, resulting in only one flexural mode near zero frequency, as expected for an ordinary plate. Nevertheless, the two birefringent flexural modes can be tuned to an arbitrarily small frequency, if needed. Moreover, by observing the eigenmodes around the Γ point, we can classify them as either in phase (labeled as F_+ modes in the first band) or out of phase (labeled as F_- modes in the second band) for the displacement field on the two arched beams. These two modes share some similarities to acoustic and optical phonons, except that both of them can actually be coupled to flexural waves in the background (as shown in Sec. IV). Full-wave simulations confirm that the main displacements of these eigenmodes are in the out-of-plane direction.

III. MEASURED DOUBLE-BIREFRINGENT FLEXURAL MODES

Next, we fabricate and experimentally measure the band structure of the birefringent flexural-wave metamaterial. The sample printed by a stereolithographic 3D printer

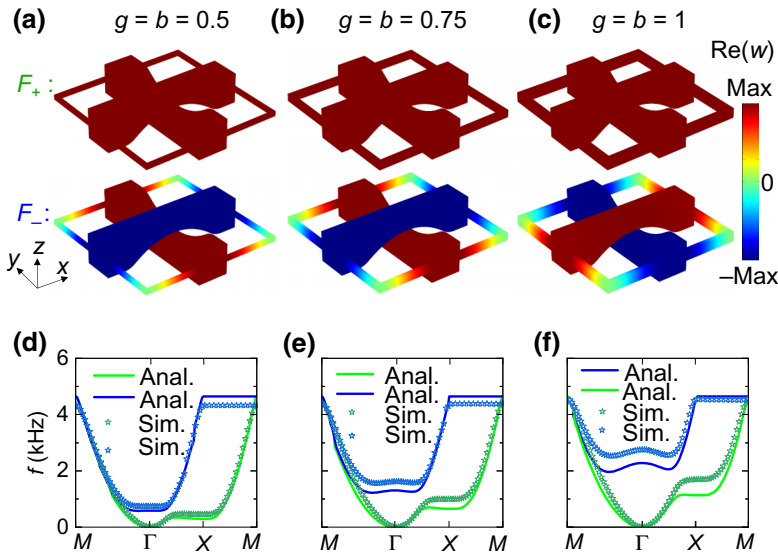


FIG. 2. (a)–(c) Field patterns $[\text{Re}(w)]$ of in-phase (F_+) and out-of-phase (F_-) flexural eigenstates around the Γ point for $g = b = 0.5$ mm (a), $g = b = 0.75$ mm (b), and $g = b = 1$ mm (c). Corresponding band structures of the first two bands with birefringent flexural waves are shown in (d)–(f), respectively. Green (blue) band plots in-phase F_+ (out-of-phase F_-) flexural modes. Lines (symbols) are model (full-wave simulation) results.

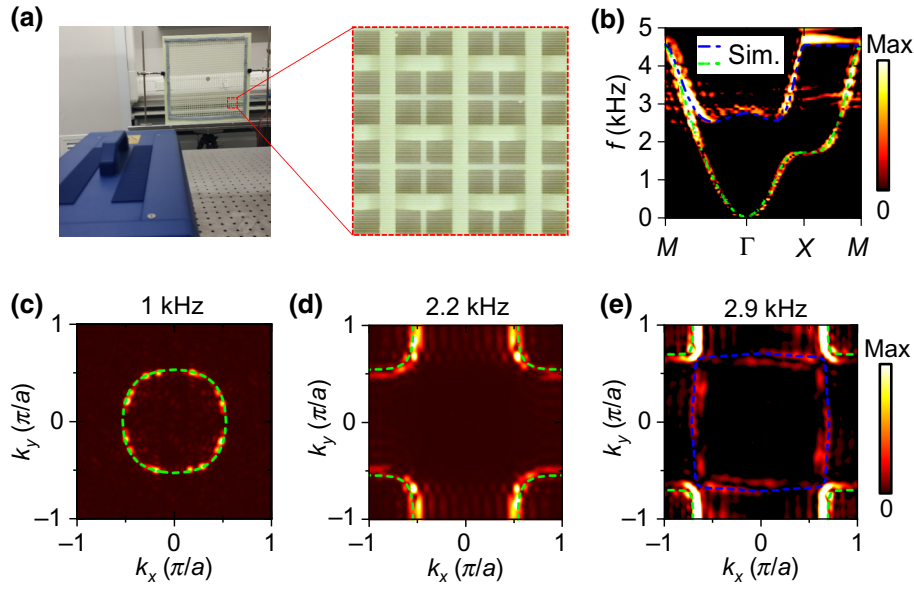


FIG. 3. Experimental band structure. (a) Flexural waves, excited by a piezoelectric transducer at the center of the metamaterial, are mapped by a scanning laser vibrometer. Inset shows 3×3 unit cells marked by a red dashed square. Blu Tack is attached to the outer boundaries of the sample to reduce reflection. (b) Color map, experimentally measured band structure by plotting the spatial and temporal Fourier-transform amplitude of the out-of-plane displacement fields. (c)–(e) Measured (color map) EFCs of the birefringent metamaterial at 1, 2.2, and 2.9 kHz, respectively. Green (blue) dashed curves are simulated results for the F_+ (F_-) modes.

(iSLA660, ZRapid Tech) is shown in Fig. 3(a), which possesses the same geometric configuration as that shown in Fig. 2(c), i.e., $g = b = 1$ mm. A piezoelectric transducer is attached to the center of the sample to excite flexural waves, while the out-of-plane displacement field is mapped by a scanning Doppler vibrometer (OptoMET, Germany). By Fourier transforming the measured field in both the spatial and temporal domains, the measured band structure is obtained and shown as a color map in Fig. 3(b). Double-birefringent flexural modes can be seen from around 2.7 to 4.5 kHz, which fall within the usual scope of a conventional effective medium. Take the double-birefringent flexural modes around 2.9 kHz as an example: the wavelength of the flexural modes in the homogeneous plate (with a thickness of 3 mm) is 57 mm, which is around 4 times the lattice constant (14 mm). For completeness, the birefringence of the metamaterial is also visualized by the equipfrequency contours (EFCs) at 1, 2.2, and 2.9 kHz, as shown in Figs. 3(c)–3(e), respectively. The band structures from full-wave simulations are plotted as green (first band, F_+) and blue dashed lines (second band, F_-), which are in excellent agreement with the experimental results. The EFCs evolve from encircling the Γ point (e.g., 1 kHz) to encircling the M point (e.g., 2.2 kHz).

IV. EXPERIMENTAL CHARACTERIZATION OF DOUBLE REFRACTION

As mentioned from our approach, the two birefringence flexural modes are both easy to couple to the flexural waves in the background plate, as there is no significant symmetry mismatch of polarization. On the other hand, the two birefringence flexural modes can be revealed through double refraction. To experimentally observe the double-refraction phenomenon, another sample is fabricated with

a slab of metamaterial in a rectangular shape and a $\Gamma - M$ interface embedded in a homogeneous background, as shown in Fig. 4(a). A piezoelectric transducer situated at the focal point of a parabolic hollow region fires a beam of planar wavefront at 3.5 kHz towards the metamaterial at an incident angle of 25° . The transmitted waves at the top region (surrounded by Blu Tack for absorption boundaries) of the metamaterial are then mapped using laser scanning vibrometry.

The simulated field pattern of the out-of-plane displacement $[\text{Re}(w)]$ at 3.5 kHz is shown in Fig. 4(b). It can be seen that the plane wave (indicated by a white arrow) is split into two beams within the metamaterial region, one for “ F_+ ” modes (green arrow) and one for “ F_- ” modes (blue arrow), and transmits into the background region as two beams. The corresponding measured result at 3.5 kHz is shown in Fig. 4(c). Two transmitted beams, indicated by green and blue arrows, can be seen in the background region and exit the slab in the same direction as the incident waves, which is in agreement with simulation results. Double refraction can be further confirmed by plotting the amplitudes of the spatial Fourier transform of the measured fields in the metamaterial region, as shown in Fig. 4(d). The white long-dash line indicates the locations for conserving the tangential wave vector at the surface in the $\Gamma - M$ direction. The experimentally observed components approximately fall along the white dashed line. The intersection of the components with the EFCs (blue and green lines) can then be used to find the two \mathbf{k} vectors (directions) of the transmitted beams through the surface normal of the EFCs. Despite the limitations on the finite size of the metamaterial region, double refraction is qualitatively demonstrated in Figs. 4(c) and 4(d), in good agreement with theoretical predictions.

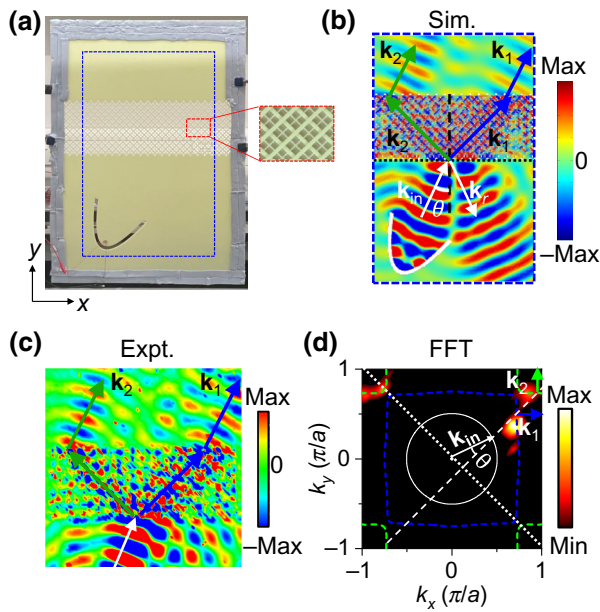


FIG. 4. Experimental double refraction. (a) A beam of planar wavefront is generated from a piezoelectric transducer on a parabolic hollow region at an incident angle of $\theta = 25^\circ$ towards the metamaterial slab. Surface normal is along the $\Gamma - M$ direction. Inset, magnification of the metamaterial region. Blu Tack is attached at the outer boundary of the background homogeneous plate (3 mm in thickness). (b) Out-of-plane displacement (w) fields from full-wave simulations at 3.5 kHz. Incident beam (white arrow) splits into two (blue and green arrows) in the metamaterial and exits as two parallel beams in the transmitted region. (c) Measured field map at 3.5 kHz. (d) Color map, Fourier-transform spectrum of the measured spatial fields. Blue and green dashed curves, simulated EFCs of the first (F_+) and second (F_-) bands. White circle, EFC of the background medium. White long-dash line, locations in conserving transverse \mathbf{k} vector.

V. CONCLUSION

We construct a metamaterial by upsetting the topology of unit cells using overpass structures with a network of beams. Such a metamaterial allows us to realize birefringence of single polarization in terms of flexural waves and in the long-wavelength regime, with experimental confirmation using the band structure and double refraction. Such birefringence, without significant symmetry mismatch between the modes, allows efficient coupling to background waves and may find potential applications in nondestructive testing and designing elastic wave components.

ACKNOWLEDGMENTS

This work is supported by the Research Grants Council of Hong Kong through Projects No. AoE/P-502/20 and No. C6013-18G.

Y.M. did the design and simulations. Y.M. and Y.H. did the experiments. Y.M. and J.L. performed the data analysis and discussion. J.L. formulated the idea and model and supervised the project. All authors revised the manuscript.

The authors declare no competing interests.

-
- [1] D. R. Smith, W. J. Padilla, D. C. Vier, S. C. Nemat-Nasser, and S. Schultz, Composite Medium with Simultaneously Negative Permeability and Permittivity, *Phys. Rev. Lett.* **84**, 4184 (2000).
 - [2] R. A. Shelby, D. R. Smith, and S. Schultz, Experimental verification of a negative index of refraction, *Science* **292**, 77 (2001).
 - [3] X. Huang, Y. Lai, Z. H. Hang, H. Zheng, and C. T. Chan, Dirac cones induced by accidental degeneracy in photonic crystals and zero-refractive-index materials, *Nat. Mater.* **10**, 582 (2011).
 - [4] W. Cai, U. K. Chettiar, A. V. Kildishev, and V. M. Shalaev, Optical cloaking with metamaterials, *Nat. Photonics* **1**, 224 (2007).
 - [5] J. Valentine, J. Li, T. Zentgraf, G. Bartal, and X. Zhang, An optical cloak made of dielectrics, *Nat. Mater.* **8**, 568 (2009).
 - [6] Q. Cheng, T. J. Cui, W. X. Jiang, and B. G. Cai, An omnidirectional electromagnetic absorber made of metamaterials, *New J. Phys.* **12**, 063006 (2010).
 - [7] Z. Liu, X. Zhang, Y. Mao, Y. Y. Zhu, Z. Yang, C. T. Chan, and P. Sheng, Locally resonant sonic materials, *Science* **289**, 1734 (2000).
 - [8] L. Fok, M. Ambati, and X. Zhang, Acoustic metamaterials, *MRS Bull.* **33**, 931 (2008).
 - [9] S. A. Cummer, J. Christensen, and A. Alù, Controlling sound with acoustic metamaterials, *Nat. Rev. Mater.* **1**, 16001 (2016).
 - [10] M. Dubois, C. Shi, X. Zhu, Y. Wang, and X. Zhang, Observation of acoustic Dirac-like cone and double zero refractive index, *Nat. Commun.* **8**, 14871 (2017).
 - [11] J. Li and C. T. Chan, Double-negative acoustic metamaterial, *Phys. Rev. E* **70**, 055602 (2004).
 - [12] Y. Ding, Z. Liu, C. Qiu, and J. Shi, Metamaterial with Simultaneously Negative Bulk Modulus and Mass Density, *Phys. Rev. Lett.* **99**, 093904 (2007).
 - [13] S. H. Lee, C. M. Park, Y. M. Seo, Z. G. Wang, and C. K. Kim, Composite Acoustic Medium with Simultaneously Negative Density and Modulus, *Phys. Rev. Lett.* **104**, 054301 (2010).
 - [14] J. Li and J. B. Pendry, Hiding under the Carpet: A New Strategy for Cloaking, *Phys. Rev. Lett.* **101**, 203901 (2008).
 - [15] J. Christensen and F. J. G. de Abajo, Anisotropic Metamaterials for Full Control of Acoustic Waves, *Phys. Rev. Lett.* **108**, 124301 (2012).
 - [16] Y. Wu, Y. Lai, and Z. Q. Zhang, Elastic Metamaterials with Simultaneously Negative Effective Shear Modulus and Mass Density, *Phys. Rev. Lett.* **107**, 105506 (2011).
 - [17] R. Zhu, X. N. Liu, G. Hu, C. T. Sun, and G. L. Huang, Negative refraction of elastic waves at the deep-subwavelength scale in a single-phase metamaterial, *Nat. Commun.* **5**, 5510 (2014).

- [18] M. Farhat, S. Guenneau, and S. Enoch, Ultrabroadband Elastic Cloaking in Thin Plates, *Phys. Rev. Lett.* **103**, 024301 (2009).
- [19] M. Farhat, S. Guenneau, and S. Enoch, Broadband cloaking of bending waves via homogenization of multiply perforated radially symmetric and isotropic thin elastic plates, *Phys. Rev. B* **85**, 020301 (2012).
- [20] N. Stenger, M. Wilhelm, and M. Wegener, Experiments on Elastic Cloaking in Thin Plates, *Phys. Rev. Lett.* **108**, 014301 (2012).
- [21] H. Zhu and F. Semperlotti, Anomalous Refraction of Acoustic Guided Waves in Solids with Geometrically Tapered Metasurfaces, *Phys. Rev. Lett.* **117**, 034302 (2016).
- [22] S. Li, D. Zhao, H. Niu, X. Zhu, and J. Zang, Observation of elastic topological states in soft materials, *Nat. Commun.* **9**, 1370 (2018).
- [23] S. Y. Yu, C. He, Z. Wang, F. K. Liu, X. C. Sun, Z. Li, H. Z. Lu, M. H. Lu, X. P. Liu, and Y. F. Chen, Elastic pseudospin transport for integratable topological phononic circuits, *Nat. Commun.* **9**, 3072 (2018).
- [24] J. Zhu, Y. Liu, Z. Liang, T. Chen, and J. Li, Elastic Waves in Curved Space: Mimicking a Wormhole, *Phys. Rev. Lett.* **121**, 234301 (2018).
- [25] Y. Liu, Z. Liang, F. Liu, O. Diba, A. Lamb, and J. Li, Source Illusion Devices for Flexural Lamb Waves Using Elastic Metasurfaces, *Phys. Rev. Lett.* **119**, 034301 (2017).
- [26] Y. Chen, M. Kadic, and M. Wegener, Roton-like acoustic dispersion relations in 3D metamaterials, *Nat. Commun.* **12**, 3278 (2021).
- [27] J. A. Martínez, M. Groß, Y. Chen, T. Frenzel, V. Laude, M. Kadic, and M. Wegener, Experimental observation of roton-like dispersion relations in metamaterials, *Sci. Adv.* **7**, eabm2189 (2021).
- [28] H. Zhu, S. Patnaik, T. F. Walsh, B. H. Jared, and F. Semperlotti, Nonlocal elastic metasurfaces: Enabling broadband wave control via intentional nonlocality, *Proc. Natl. Acad. Sci. U. S. A.* **117**, 26099 (2020).
- [29] R. Zhu, H. Yasuda, G. L. Huang, and J. K. Yang, Kirigami-based elastic metamaterials with anisotropic mass density for subwavelength flexural wave control, *Sci. Rep.* **8**, 483 (2018).
- [30] Y. Liu, Z. Liang, J. Zhu, L. Xia, O. Mondain-Monval, T. Brunet, A. Alù, and J. Li, Willis Metamaterial on a Structured Beam, *Phys. Rev. X* **9**, 011040 (2019).
- [31] A. S. Gliozzi, M. Miniaci, A. Chiappone, A. Bergamini, B. Morin, and E. Descrovi, Tunable photo-responsive elastic metamaterials, *Nat. Commun.* **11**, 2576 (2020).
- [32] H. Pinto and R. Jones, Theory of the birefringence due to dislocations in single crystal CVD diamond, *J. Phys.: Condens. Matter* **21**, 364220 (2009).
- [33] M. Lejman, G. Vaudel, I. C. Infante, I. Chaban, T. Pezeril, M. Edely, G. F. Nataf, M. Guennou, J. Kreisel, V. E. Gusev, *et al.*, Ultrafast acousto-optic mode conversion in optically birefringent ferroelectrics, *Nat. Commun.* **7**, 12345 (2016).
- [34] N. Yu and F. Capasso, Flat optics with designer metasurfaces, *Nat. Mater.* **13**, 139 (2014).
- [35] D. Lin, P. Fan, E. Hasman, and M. L. Brongersma, Dielectric gradient metasurface optical elements, *Science* **345**, 298 (2014).
- [36] A. Arbabi, Y. Horie, M. Bagheri, and A. Faraon, Dielectric metasurfaces for complete control of phase and polarization with subwavelength spatial resolution and high transmission, *Nat. Nanotechnol.* **10**, 937 (2015).
- [37] M. Khorasaninejad, W. T. Chen, R. C. Devlin, J. Oh, A. Y. Zhu, and F. Capasso, Metalenses at visible wavelengths: Diffraction-limited focusing and subwavelength resolution imaging, *Science* **352**, 1190 (2016).
- [38] J. P. Balthasar Mueller, N. A. Rubin, R. C. Devlin, B. Groever, and F. Capasso, Metasurface Polarization Optics: Independent Phase Control of Arbitrary Orthogonal States of Polarization, *Phys. Rev. Lett.* **118**, 113901 (2017).
- [39] Z. Shi, A. Y. Zhu, Z. Li, Y. W. Huang, W. T. Chen, C. W. Qiu, and F. Capasso, Continuous angle-tunable birefringence with freeform metasurfaces for arbitrary polarization conversion, *Sci. Adv.* **6**, 3367 (2020).
- [40] G. Shabtay, E. Eiding, Z. Zalevsky, D. Mendlovic, and E. Marom, Tunable birefringent filters-optimal iterative design, *Opt. Express* **10**, 1534 (2002).
- [41] G. S. Lobov, A. Marinins, S. Etcheverry, Y. Zhao, E. Vasileva, A. Sugunan, F. Laurell, L. Thylén, L. Wosinski, M. Östling, M. S. Toprak, and S. Popov, Direct birefringence and transmission modulation via dynamic alignment of P3HT nanofibers in an advanced opto-fluidic component, *Opt. Mater. Express* **7**, 52 (2017).
- [42] H. M. Kim, T. H. Kim, B. Kim, and Y. Chung, Temperature-insensitive torsion sensor with enhanced sensitivity by use of a highly birefringent photonic crystal fiber, *IEEE Photonics Technol. Lett.* **22**, 1539 (2010).
- [43] M. Lu, C. Zhang, L. Feng, J. Zhao, Y. Chen, Y. Mao, J. Zi, Y. Zhu, S. Zhu, and N. Ming, Negative birefringence of acoustic waves in a sonic crystal, *Nat. Mater.* **6**, 744 (2007).
- [44] F. Zangeneh-Nejad and R. Fleury, Acoustic birefringence via non-Eulerian metamaterials, *J. Appl. Phys.* **126**, 034902 (2019).
- [45] S. Wang, G. Zhang, X. Wang, Q. Tong, J. Li, and G. Ma, Spin-orbit interactions of transverse sound, *Nat. Commun.* **12**, 6125 (2021).
- [46] H. Zhu, S. Patnaik, T. F. Walsh, B. H. Jared, and F. Semperlotti, Enabling broadband wave control via intentional nonlocality, *Proc. Natl. Acad. Sci. U. S. A.* **117**, 26099 (2020).
- [47] X. Wu, Y. Meng, Y. Hao, R. Y. Zhang, J. Li, and X. Zhang, Topological Corner Modes Induced by Dirac Vortices in Arbitrary Geometry, *Phys. Rev. Lett.* **126**, 226802 (2021).